

PPPL-5378

Energy Exchange Dynamics across L-H Transitions in NSTX

A. Diallo and S.J. Zweben

March 2017



Prepared for the U.S. Department of Energy under Contract DE-AC02-09CH11466.

Princeton Plasma Physics Laboratory

Report Disclaimers

Full Legal Disclaimer

This report was prepared as an account of work sponsored by an agency of the United States Government. Neither the United States Government nor any agency thereof, nor any of their employees, nor any of their contractors, subcontractors or their employees, makes any warranty, express or implied, or assumes any legal liability or responsibility for the accuracy, completeness, or any third party's use or the results of such use of any information, apparatus, product, or process disclosed, or represents that its use would not infringe privately owned rights. Reference herein to any specific commercial product, process, or service by trade name, trademark, manufacturer, or otherwise, does not necessarily constitute or imply its endorsement, recommendation, or favoring by the United States Government or any agency thereof or its contractors or subcontractors. The views and opinions of authors expressed herein do not necessarily state or reflect those of the United States Government or any agency thereof.

Trademark Disclaimer

Reference herein to any specific commercial product, process, or service by trade name, trademark, manufacturer, or otherwise, does not necessarily constitute or imply its endorsement, recommendation, or favoring by the United States Government or any agency thereof or its contractors or subcontractors.

PPPL Report Availability

Princeton Plasma Physics Laboratory:

<http://www.pppl.gov/techreports.cfm>

Office of Scientific and Technical Information (OSTI):

<http://www.osti.gov/scitech/>

Related Links:

[U.S. Department of Energy](#)

[U.S. Department of Energy Office of Science](#)

[U.S. Department of Energy Office of Fusion Energy Sciences](#)

Energy Exchange Dynamics across L-H Transitions in NSTX

A. Diallo¹, S. Banerjee², S.J. Zweben¹, and T. Stoltzfus-Dueck¹

¹ Princeton Plasma Physics Laboratory, Princeton University, NJ, USA.

² Institute for Plasma Research, Bhat, Gandhinagar 382428, Gujarat, India.

February 24, 2017

Abstract:

We studied the energy exchange dynamics across the low-to-high-confinement (L-H) **transition** in NSTX discharges using the gas-puff imaging (GPI) diagnostic. The investigation focused on the energy exchange between flows and turbulence, to help clarify the mechanism of the L-H transition. We apply this study to three type of heating schemes, including a total of 17 shots from the NSTX 2010 campaign run. Results show that the edge fluctuation characteristics (fluctuation levels, radial and poloidal correlation lengths) measured using GPI do not vary just prior to the H-mode transition, but change after the transition. Using a velocimetry approach (orthogonal-dynamics programming), velocity fields of a 24×30 cm GPI view during the L-H transition were obtained with good spatial (~ 1 cm) and temporal ($\sim 2.5 \mu\text{s}$) resolutions. Analysis using these velocity fields shows that the production term is systematically negative just prior to the L-H transition indicating transfer from mean flows to turbulence, which is inconsistent with the predator-prey paradigm. **Moreover, the inferred absolute value of the production term is two orders of magnitude too small to explain the observed rapid L-H transition.** These discrepancies are further reinforced by consideration of the ratio between the kinetic energy in the mean flow to the thermal free energy, which is estimated to be much less than 1, suggesting again that turbulence depletion mechanism may not be playing an important role in the transition to the H-mode. Although the **Reynolds work therefore appears to be too small** to directly deplete the turbulent free energy reservoir, order-of-magnitude analysis shows that the Reynolds stress may still make a non-negligible contribution to the observed poloidal flows.

1 Introduction

Since the discovery of the high confinement (referred to as H-mode) regime in the ASDEX tokamak [1, 2], it has become the standard mode of operation of present tokamaks and is planned for future fusion devices such as ITER. This H-mode is associated with the formation of an edge transport barrier that causes a transition from a low (L) to high (H) confinement regime, resulting in improved performance (i.e., temperature, density, and energy confinement time). Operationally, the L-H transition occurs when the injected heat (beam, radio frequency waves, and/or ohmic) exceeds a threshold. The physics governing

8 this transition is, however, unclear, and remains one of the open issues in fusion research. 8

9 Most theoretical descriptions of the L-H transition are based on the shear of the radial electric field 9
 10 and coincident $\mathbf{E} \times \mathbf{B}$ poloidal flow shear, which is thought to be responsible for the onset of the anoma- 10
 11 lous transport suppression [3]. First introduced by Ref. [4], it is generally supposed that stabilization 11
 12 of anomalous transport can be achieved by the flow shear via the breaking and/or distortion of edge 12
 13 turbulence eddies. Later, a self-consistent model of the L-H transition was derived from coupled non- 13
 14 linear envelope equations for the fluctuation level and E_r' [5]. This derived model is a paradigm that 14
 15 is referred to as the predator-prey model. *The key point of this model is that there is nonlinear energy 15*
 16 *transfer from turbulence to flows via the Reynolds stress. This transfer drives a sheared zonal $\mathbf{E} \times \mathbf{B}$ flow,* 16
 17 *and concurrently directly depletes the turbulent fluctuations.* Alternatively, the contribution of ∇p_i to E_r 17
 18 **can also drive** the sheared zonal $\mathbf{E} \times \mathbf{B}$ flows. Depending on the model, turbulence suppression is either due 18
 19 to direct depletion by the Reynolds-stress-induced energy transfer or due to the $\mathbf{E} \times \mathbf{B}$ shearing of eddies, 19
 20 which **can in theory** reduce the effective growth rate and increase the damping of the turbulent 20
 21 fluctuations. Overall, in the models described above, turbulence suppression is thought to trigger the 21
 22 L-H transition. 22

23 Experimentally, several machines (EAST [6], DIII-D [7], C-Mod [8], and HL-2A [9]) have found 23
 24 that turbulence driven mean flows enhance the edge shear flow, which was thought to trigger the L-H 24
 25 transition, essentially consistent with the predator-prey paradigm. However, similar investigations of 25
 26 energy transfer between perpendicular flows and turbulence in the plasma boundary region of the JET 26
 27 tokamak (in ohmic and diverted discharges) have shown that the energy transfer from the zonal flows to 27
 28 turbulence can be both positive and negative in the proximity of sheared flows [10]. Although the latter 28
 29 work was not applied to the L-H transition, it suggests as an example that the turbulence can be either 29
 30 pumped or depleted by the sheared flows, pointing to possible ambiguity in using the energy transfer as 30
 31 a key mechanism in the studies. 31

32 In this paper, we analyze the L-H transition dynamics on NSTX using the velocimetry of 2-D edge tur- 32
 33 bulance data from gas-puff imaging (GPI). More specifically, we describe turbulence correlation analyses 33
 34 and determine the velocity components at the edge across the L-H transition for 17 discharges with three 34
 35 types of heating power (neutral beam injection - NBI, ohmic, and radio frequency - RF). The turbulence 35
 36 dynamics are examined and the energy transfer between turbulence and mean flow is computed. Using 36
 37 a reduced model equation of edge flows and turbulence, the energy transfer dynamics is compared with 37
 38 the turbulence depletion hypothesis of the predator-prey model of the L-H transition. 38

39 2 Underlying model equations 39

40 Our analysis will rest on a *minimal model* of edge turbulence and sheared flows, using the very simple 40
 41 two-fluid flux-tube equations of Ref. [11], which make the following assumptions: isothermal electrons; 41

is approximately equal to $E_{\tilde{n}}$ for the typical edge turbulence case $k_{\perp}\rho_s \sim 0.1$. On timescales faster than poloidal rotation damping, this requires

$$\frac{E_z}{E_{\tilde{n}}} = \frac{\int dV \langle v_E^y \rangle^2 / c_s^2}{\int dV \tilde{n}_e^2 / n_0^2}, \quad (5)$$

to be order unity, with $E_{\tilde{n}}$ evaluated immediately pre-transition and using the increase in E_z over the transition^{2 3}.

To determine the evolution of the flow shear, we may use the zonal vorticity equation

$$n_0 m_i \partial_t \partial_x \langle v_E^y \rangle = -n_0 m_i \partial_x^2 \langle \tilde{v}_E^x \tilde{v}_E^y \rangle - T_{e0} B \partial_x \langle \mathcal{K}^x n_e \rangle, \quad (6)$$

showing that up to a spatially constant (but possibly time-dependent) offset, the poloidal rotation evolves in response to the Reynolds stress divergence (i.e., $\partial_x \langle \tilde{v}_E^x \tilde{v}_E^y \rangle$), along with a curvature term that mediates poloidal rotation damping. Since poloidal rotation is typically damped towards its neoclassical value at a rate of order the ion transit frequency $\nu \sim v_{ti}/qR$ [14, 15] the Reynolds stress contribution to the poloidal rotation may be very crudely estimated from Eq. 6 as $\langle v_E^y \rangle \sim -\nu^{-1} \partial_x \langle \tilde{v}_E^x \tilde{v}_E^y \rangle \sim -(qR/v_{ti}) \partial_x \langle \tilde{v}_E^x \tilde{v}_E^y \rangle$. Although this estimate is too rough for detailed quantitative comparison, it is adequate for an order-of-magnitude check.

In principle, the flux surface average is a poloidal and toroidal average over an entire flux surface. However, since the gas-puff imaging (GPI) diagnostic only views a small fraction of the surface (see Sec. 3 below for details), the poloidal spatial average over the GPI view is a poor approximation to the total flux-surface average. For this reason, we estimate the flux-surface average of velocity with a combination of a poloidal average (across the field of view) and a low-pass frequency filter (here, a cutoff at 1 kHz was used), exploiting a typical separation in frequency scales between the slow temporal evolution of the zonal component and the fast temporal evolution of the turbulent fluctuations.

ρ_s , choose the slowest of the following three rates: collisional parallel electron diffusion $\sim k_{\parallel}^2 v_{te}^2 / k_{\perp}^2 \rho_s^2 \nu_{ei}$, free/collisionless parallel electron flow $\sim k_{\parallel} v_{the} / k_{\perp} \rho_s$, or shear Alfvén/electromagnetic $\sim k_{\parallel} v_A$. For our parameters, these rates are about $5.5 \cdot 10^7 \text{s}^{-1}$, $4.8 \cdot 10^6 \text{s}^{-1}$, and $2.6 \cdot 10^5 \text{s}^{-1}$, respectively, all much more rapid than the L-H transition.

²Resistive dissipation implies that the transfer of energy from E_n to E_{\sim} is at least somewhat lossy. However, even in a strongly nonadiabatic case where $\tilde{h}_e \doteq \tilde{n}_e/n_0 - e\tilde{\phi}/T_{e0}$ is comparable in magnitude with $e\tilde{\phi}/T_{e0}$, the resistive dissipation $\eta j_{\parallel}^2 = j_{\parallel} \nabla_{\parallel} (T_{e0} \tilde{h}_e / e)$ is only of comparable size with the energy transfer into $E_{\sim} [j_{\parallel} \nabla_{\parallel} \tilde{\phi}]$. So, even in that case, the predator-prey model requires $E_z/E_{\tilde{n}} \sim 1/2 \sim O(1)$.

³On slow enough timescales, Eq. (5) is modified by poloidal rotation damping. Modeling the curvature term in Eq. (3) as $-\nu E_z$ for a poloidal rotation damping rate ν around v_{ti}/qR , we can time-integrate energy balance over the L-H transition

$$-\Delta|_{\text{R.S.}}(E_n + E_{\sim}) = \int dt \int dV n_0 m_i (\tilde{v}_E^x \tilde{v}_E^y) \partial_x \langle v_E^y \rangle = \Delta E_z + \int dt \nu E_z,$$

where Δ indicates H-mode value minus L-mode value and subscript R.S. means “due to Reynolds stress.” To roughly estimate the effect of Reynolds stress, we may take $\int dt \nu E_z \rightarrow (\nu \tau_{\text{L-H}}) E_z$. In our data, $(\nu \tau_{\text{L-H}}) \lesssim 1$, so poloidal flow damping may relax Eq. (5) only by roughly a factor of 2.

3 Experimental Approach

Since gas-puff imaging is central to the analysis described here, we provide a brief description of the GPI system on NSTX. We refer the reader to a more extensive description of the GPI diagnostics elsewhere [16, 17]. GPI diagnostics are used to image the turbulent fluctuations in the edge of fusion devices. This diagnostic in NSTX relies on a deuterium gas puff into the plasma via a gas manifold. The visible neutral line emission of D_α at 656 nm from the cloud is then imaged using a fast framing camera. The camera views are aligned with magnetic field pitch angle of ~ 36 degrees, which enables optimum spatial resolution in the radial vs. binormal plane, where the binormal direction is the perpendicular to the magnetic field within the flux surface. The GPI field of view is centered 20 cm above the outer midplane spanning the separatrix. This view spans a region of 24 cm by 30 cm (radial and poloidal directions) with a spatial resolution of ~ 1 cm at 400 kHz sampling rate. The directions x, y labeled in the above section correspond, respectively, to radial r and poloidal θ in the remainder of the text. For the study presented below, the collected images are normalized by time-averaged images and then analyzed for the spatial correlations (radial and poloidal lengths). Furthermore, these images are processed using velocimetry techniques to determine the velocity fields and to compute the various terms in the model equations highlighted in Sec. 2 in order to test the L-H models.

Turbulence Characteristics

Edge turbulence characteristics across L-H transitions in NSTX were described previously using GPI data taken in 2009 [18], and the present database from 2010 shows the same general characteristics. The most dramatic change at the L-H transition is a rapid reduction in relative GPI light fluctuation levels (\tilde{I}/\bar{I}) inside and near the separatrix (\tilde{I} is the rms fluctuations and \bar{I} is the mean intensity fluctuations of the GPI signal), which occurs within $\sim 100 \mu\text{s}$ of the L-H transition time as seen in the standard D_α diagnostics.

Examples of the radial profiles of the GPI signal level and its relative fluctuation level just before and after the L-H transition are shown in Fig. 1. It is clear from this figure that the average GPI signal's intensity radial profile shift inward in the H-mode phase. In this phase, the fluctuation levels drop inside the separatrix relative to the L-mode phase. **Furthermore, Fig. 1(b) indicates that the maximum level of fluctuations L-mode occurs near 1 cm inside the separatrix.**

Figure 2(a) shows the time dependence of the relative GPI fluctuation level averaged over all 17 shots in the present database (see table I), at the location 1 cm inside the separatrix. These times are measured with respect to the time at which the GPI fluctuation level **transitions to** the H-mode state in each shot, which has an uncertainty of about ± 0.1 ms. There is no significant time variation in the relative fluctuation level during the ~ 3 ms preceding the transition, and the sudden drop at the transition from

($\tilde{I}/\bar{I} \sim 25\%$ to $\sim 15\%$ occurs consistently over ~ 0.1 ms. Note that the shot-to-shot variations during the L-mode period, in Fig. 2(a), are $\sim 4\%$ in \tilde{I}/\bar{I} .

Figures 2(b) and 2(c) display the time history of the radial (L_{rad}) and poloidal (L_{pol}) lengths (FWHM) across the L-H transition at 1 cm inside the separatrix. There is no significant change in the average poloidal or radial correlation lengths during the ~ 3 ms preceding the transition. However, there is a significant increase in the average poloidal correlation length, and a decrease in the average radial correlation length **over** the ~ 1 ms period after the transition. The shot-to-shot variations in during the L-mode period are ± 1.0 cm in the poloidal correlation length and ± 1.2 cm in the radial correlation length.

The poloidal and radial turbulence velocities were also evaluated using the same time-delayed cross-correlation technique as in Ref. [18]. These velocities were evaluated at each radius vs. time by averaging over $\pm 30 \mu\text{s}$, then averaged over 22 cm poloidally within the GPI image. Results for 1 cm inside the separatrix are shown for all the shots from table I in Fig. 3, along with the shot averages in black. There was a considerable spread in velocities from shot-to-shot, but the shot-averaged velocities did not vary significantly vs. time during the 3 ms before the L-H transitions (at least above about ± 1 km/s). Across the L-H transition there seems to be an increase in the shot-averaged poloidal velocity from -0.8 km/s to $+0.4$ km/s (toward the electron diamagnetic drift direction), and a slight decrease in the shot-averaged radially outward velocity from 0.7 km/s to 0.6 km/s. Overall, within the error bars, there is no clear observation of an L-H transition trigger.

Some of the variation in the poloidal velocity for individual shots in Fig. 3 prior to the L-H transition is due to a poloidally oscillating “zonal flow” described earlier for GPI in NSTX [18, 19]. An example of these poloidal flow oscillations for one shot is shown in Fig. 4, in which the time evolution of the poloidal velocity is plotted in color vs. the radial and poloidal coordinates. Such zonal flows in NSTX can extend across most of the poloidal range of the GPI view, and over the radial range near and inside the separatrix. As seen previously [18, 19], these oscillations are found in the frequency range $\sim 2 - 5$ kHz during the 30 ms preceding the L-H transition for most (but not all) of the shots in table I. However, there is no systematic increase in the amplitude of these flows just prior to the L-H transition, and in some cases similar flows also exist after the L-H transition. Further analysis of these flows is interesting but beyond the scope of the present paper.

Application of velocimetry to GPI

To evaluate the energy exchange dynamics using GPI, we use high resolution velocimetry to measure the local 2D turbulence motion, and assume that the turbulence motion is equivalent to the local $\mathbf{E} \times \mathbf{B}$ fluid motion. This is a common assumption in the analysis of GPI [8], beam-emission-spectroscopy (BES) [20], and Doppler reflectometry diagnostics of edge turbulence [21], **but is only approximately**

157 **true due to polarization effects at small scales and possible contributions of the parallel** 157
 158 **electron heat flux.** There are also systematic limitations and uncertainties in any velocimetry analy- 158
 159 GPI data, such as the well-known “barber-pole” effect, as discussed in [22, 23]. **Both of these** 159
 160 **uncertainties are special cases of a more general limitation, namely that velocimetry tech-** 160
 161 **niques only see velocities parallel to the intensity gradient. Therefore, velocities along exact** 161
 162 **isocontours of intensity are invisible, although small intensity fluctuations can be tracked** 162
 163 **successfully given a sufficient signal/noise level.** This is an unavoidable ambiguity that is shared by 163
 164 GPI velocimetry, BES velocimetry, and any other analogous techniques. Such ambiguity is particu- 164
 165 larily evident in the H-mode phase where **where the images sometimes have very low fluctuation levels.** 165

166 To extract the time varying 2D velocity field $\mathbf{v}(r, \theta, t)$ from the intensity fluctuations recorded with the 166
 167 GPI diagnostic, we use the orthogonal dynamic programming (ODP) technique. The ODP technique is 167
 168 described in detail in Ref. [24] and the salient features are only discussed briefly here. ODP is a robust 168
 169 technique for searching optical alignments of patterns through the simple realization of cross correlation. 169
 170 The procedure is essentially the search of a transformation that relates the consecutive image with the 170
 171 previous image in a time series and minimizes the Minkowski distance $L_n = \sum_i \sum_j |I_0(i, j) - I_1(i, j)|^n$ 172
 173 between them. The key feature of the algorithm is to reduce the problem of determining 2D displacements 173
 174 into a series of 1D displacements selected carefully to reduce the complexity of the task. Each image 174
 175 of the temporally separated pair is sliced into several parallel overlapping strips (here along r direction) 175
 176 as shown in Fig.1 of Ref. [24]. The velocity is estimated from the distortion or transformation, in the 176
 177 slicing direction, necessary to minimize the calculated intensity difference. The whole process is iterated 177
 178 several times to achieve higher spatial resolution similar to the actual pixel resolution of the image. The 178
 179 width of the strips and the corresponding overlaps are reduced by about $\sqrt{2}$ in each radial-poloidal (r - θ) 179
 180 iteration. 180

181 *This technique has the merit of determining the velocity field at the sampling time and with spatial* 181
 182 *resolution close to that of the images, which are advantages over the commonly used time-delay estimate* 182
 183 *(TDE) velocity estimates.* It is worth noting that ODP showed overall good agreement ($\sim 80\%$ corre- 183
 184 lations) when compared against the commonly used time-delay estimate (TDE) velocity reconstruction, 184
 185 **which has a much longer ($\sim 30 \mu s$) time resolution.** Similarly, ODP was also compared with spatial 185
 186 Fourier harmonics approach (to be described elsewhere) and showed $\sim 80\%$ correlation. For the remainder 186
 187 of the paper, **only** the velocimetry using the ODP will be discussed. Displayed in Fig. 5 is an example of the 187
 188 ODP 2D reconstructions of the velocity data. 188

189 Previous probe measurements of the energy transfer [6, 9] **faced several challenges**, mainly due to the 189
 190 spatial undersampling of the region of interest. GPI offers more spatial points than probes do, reducing this 190
 191 challenge. Here, we compute the Reynolds stress ($\langle \tilde{v}_\theta \tilde{v}_r \rangle$) and the production term 191

($\langle \tilde{v}_\theta \tilde{v}_r \rangle \partial_r \langle \bar{v}_\theta \rangle$) to qualitatively provide the energy transfer direction during L-H transition. **All operations are defined in the next section.** The key metric is the energy transfer between mean flows to turbulence, which is directly related to the momentum flux and the radial gradient in the mean flow (i.e., the production term). This quantity can be either positive (from turbulence to driven flows) or negative (from DC (zonal) flows to turbulence).

Energy transfer computations: Results

We have computed the 2D velocity data $\mathbf{v} = \bar{\mathbf{v}} + \tilde{\mathbf{v}}, \forall (r, \theta, t)$, where r represents the radius, θ describes the poloidal direction, and t is the time. Figures 6 to 8 show the flow velocities and derived parameters, namely, the poloidally averaged poloidal flow, its shear, the Reynolds stress, and the production term, for three types of heating schemes. For these figures, all these quantities are computed at radial position 1 cm inside the last closed flux surface, **which, in addition to being where the maximum fluctuation level of fluctuations occur (see Fig. 1 (b)), is typically the center of the 2 - 3 cm wide pedestal gradient region most relevant for the study of the L-H transition in NSTX (see figure 6 in Ref. [25]).** The shaded area in each panel around each solid line represents the standard deviations for all discharges of the same heating scheme. For instance, in NBI case, we only choose the discharges in table I with NBI heating and average over them. The horizontal axis represents the time relative to the L-H transition where “t=0” indicates the L-H transition determined with 100 μ s uncertainty. A 1 kHz cutoff was applied to the raw velocity profiles to separate the mean flow from the fluctuating flow. More specifically, the mean flow ($\bar{\mathbf{v}}$) is given by low-pass filtering the raw velocity at 1 kHz and the fluctuating component of the flow ($\tilde{\mathbf{v}}$) is given by high-pass filtering the raw velocity. This cutoff frequency was chosen to include the poloidally oscillating flow (2 - 5 kHz) described in Refs. [18, 19] into the non zonal component. **Such approach was also used in the analysis of Ref. [8]. Note that choosing an alternate cutoff frequency that includes the poloidal oscillation in the zonal component does not qualitatively change the results presented in this paper.** The angular brackets ($\langle \dots \rangle$) define the poloidal-average over the 22 cm (GPI view) instead of the flux average (see the end of Sec. 2 where a justification is provided).

In the RF and Ohmic cases, the total poloidal flow averaged poloidally (figs. 7(a) & 8(a)) becomes positive (i.e., in the electron diamagnetic drift direction) after the L-H transition. The NBI case (Fig. 6(a)) show no *significant* change before and after the L-H transition. In all three type of heating schemes, the magnitude of the shear in the mean poloidal velocity *decreases* after the L-H transition (panels (b) of figs. 6 to 8). Note that it is the absolute value of the shear that is responsible for shearing apart the eddies. For all heating schemes, this decreasing absolute value of the shear across the L-H transition is inconsistent with the idea that flow shear is suppressing the turbulence as described in Ref. [4]. However, GPI emission bands become radially narrow across the L-H transition and the fluctuation level drops in H-mode. **So it is possible that the decrease in our inferred flow shear in H-mode might be a result of**

227 **the low fluctuation level, and consequent difficulty in evaluating velocity in our analysis.** 227

228 Below, we now show three different approaches for testing the energy exchange dynamics across the L- 228
 229 H transition. First, we look at the exchange dynamics using the Reynolds stress and production term. 229
 230 Panels (c) & (d) of figs. 6 to 8 display the Reynolds stress and production term across the L-H transition at 230
 231 1 cm inside the separatrix. In these figures, the Reynolds stress and production term clearly decrease to a 231
 232 mean value of zero in H-mode. In addition, the rms fluctuations of the Reynolds stress, as well as that of the 232
 233 production term, are significantly reduced in the H-mode phase compared to the L-mode phase. **Unlike** 233
 234 **the results of Ref. [8], there is no systematic peaking of the Reynolds stress, except in the NBI** 234
 235 **case (Fig. 6(b)) prior to the L-H transition.** 235

236 Further, contrary to expectations of the predator-prey model's predictions, we systematically observe a 236
 237 negative production term just prior to the L-H transition 1 cm inside the separatrix, suggesting a transfer of 237
 238 energy from mean flows to turbulence. Despite this implication that shear flows are apparently exciting the 238
 239 turbulence, Fig. 2 shows the turbulence levels to drop across the L-H transition. These observations can 239
 240 only be reconciled if a different term in the energy balance equations becomes strongly negative at the L-H 240
 241 transition, overwhelming the Reynolds work to cause turbulence suppression. 241

242 Second, to address the above point, we recall from Sec. 2 and Ref. [11] that for the energy transfer 242
 243 to mean flows to contribute significantly to the depletion of the turbulence the condition $\frac{\langle \bar{v}_\theta \rangle^2 / c_s^2}{(\tilde{n}_e / n_{e0})^2} \gtrsim 1$ 243
 244 is required. Note that $(\tilde{n}_e / n_{e0})^2$ is that of the L-mode phase so that the ratio to be compared becomes 244
 245 $\eta \doteq \frac{\langle \bar{v}_\theta \rangle^2 / c_s^2}{\langle \tilde{I}^2 \rangle_{[L]} / \bar{I}^2}$, where $(\tilde{n}_e / n_{e0}) \sim \tilde{I} / \bar{I}$, and $\langle \tilde{I}^2 \rangle_{[L]}^{1/2}$ is the rms of the GPI intensity fluctuations over 245
 246 the L-mode phase at a given radius. Figures 9(a), 10(a), and 11(a) display **the time-dependent radial** 246
 247 **profiles of this energy ratio** for the three types of heating schemes across the L-H transition. These 247
 248 figures show that the kinetic energy in the mean flow (proportional to $\langle \bar{v}_\theta \rangle^2 / c$) remains much smaller than 248
 249 the thermal free energy (proportional to $(\tilde{n}_e / n_{e0})^2$) **at all radii with clear GPI signals.** Note that the 249
 250 radial structure of the energy ratio in the L-mode phase is shifted inward during the H-mode phase. The 250
 251 two order magnitude difference (see figs. 9 to 11) in the energies substantiates the argument that the energy 251
 252 associated with the mean flow is unable to account for the depletion of the turbulence energy, **even** 252
 253 **allowing for some order-unity inaccuracy due to resistivity, poloidal flow damping, and** 253
 254 **approximations made in the theoretical model.** As stated above the depletion is the fundamental 254
 255 aspect of the predator-prey model, resulting in a discrepancy with our data. In other words, the energy 255
 256 transfer due to **Reynolds stress appears much too small to directly deplete the energy in the** 256
 257 **turbulence.** 257

258 Third, we examine how long would the L-H transition take given this production term. We refer to 258
 259 this production generated L-H transition time as τ_{L-H}^{RS} . We estimate this by taking the ratio $\tau_{L-H}^{RS} =$ 259
 260 $E_{\tilde{n}} / (n_0 m_i \langle \tilde{v}_\theta \tilde{v}_r \rangle \partial_r \langle \bar{v}_\theta \rangle) \Leftrightarrow \tau_{L-H}^{RS} = 0.5 c_s^2 (\tilde{n}_e / n_{e0})^2 / (\langle \tilde{v}_\theta \tilde{v}_r \rangle \partial_r \langle \bar{v}_\theta \rangle)$, where $E_{\tilde{n}} \doteq$ 260
 261 $(n_0 T_{e0} / 2) (\tilde{n}_e / n_0)^2$. Assuming typical separatrix electron temperature $T_e \sim 60\text{eV}$, $(\tilde{n}_e / n_{e0}) \sim 0.25$ (see 261

figure 2(a) just prior to the L-H transition), and the production term given by panels (d) of figs. 6 to 8 of about $5 \cdot 10^9 \text{ m}^2/\text{s}^3$, we get a dimensional time indicating that the L-H transition duration τ_{L-H}^{RS} should be about 18 ms, which is far too long compared to the observed time of $\tau_{L-H}^{exp} \sim 100 \text{ } \mu\text{s}$ based on the fluctuations drop. This suggests that a much larger production term would be necessary to explain the typical L-H transition times.

Another way to look at this is to compare the production term (P) to the change in the thermal free energy (P_0) between the L and H mode phases. For the production term to be large enough to deplete the turbulence energy, the ratio $\frac{P}{P_0} \doteq \frac{n_0 m_i (\tilde{v}_E^x \tilde{v}_E^y) \partial_x \langle v_E^y \rangle}{(\tau_{L-H}^{exp})^{-1} (E_{\tilde{n}}|_L - E_{\tilde{n}}|_H)}$ should be order unity. Here τ_{L-H}^{exp} is the L-H duration time (approximately $100 \text{ } \mu\text{s}$), and $n_0 m_i (\tilde{v}_E^x \tilde{v}_E^y) \partial_x \langle v_E^y \rangle$ is the production term. $E_{\tilde{n}}|_L$ and $E_{\tilde{n}}|_H$ represent the thermal free energy averaged in the L and H phases, respectively. Here, $(\tilde{n}/n_0)^2$ is approximated by $(\tilde{I}_{gpi}/\bar{I}_{gpi})^2$. An example of such ratio is given in figure 12 for **the ohmic case 1 cm inside the separatrix (RF and NBI cases are not shown here - both give similar less than unity ratios)**. This figure shows that this ratio is always two order of magnitude less than 1, demonstrating again that the turbulence depletion by direct energy transfer into the mean flow is an unlikely mechanism for the L-H transition.

Can the Reynolds stress contribute, however, to the mean flow itself? Here, we estimate the Reynolds-stress-driven flows and compare it to the measured mean flows. Under the assumptions highlighted in Sec. 2, one can crudely estimate the contribution of the Reynolds stress to the poloidal flow by estimating from experimental data $\langle \bar{v}_\theta \rangle^{RS} \sim -qR \frac{\partial_r \langle \bar{v}_\theta \bar{v}_r \rangle}{v_{this}}$, where q is the safety factor, and v_{this} is the ion thermal velocity.

Figure 13 displays the estimated Reynolds stress contribution to the mean poloidal flow at four radii, which is compared with the GPI measured mean poloidal flow. This figure shows that both the Reynolds stress-driven mean flow (red curve) and the measured mean flow (blue curve) are of the same order of magnitude. This suggests that the contribution of the Reynolds stress to the mean flow cannot necessarily be discarded. [This is not inconsistent with the fact that Reynolds work is unable to deplete the turbulence free energy, since the turbulence free energy is much larger than the kinetic energy of the mean poloidal flows.] Note that given how crudely we estimate the contribution of the Reynolds stress, it is difficult to claim any consistency better than an order of magnitude.

4 Summary

We described detailed analyses of the energy dynamics during the L-H transition in NSTX over a database of 17 discharges spanning three heating schemes (NBI, ohmic, and RF). These analyses utilized the GPI data for determining the velocity fields using the ODP velocimetry approach. We used a minimal model [11] of edge turbulence and sheared flows to describe the transfer of energy between turbulence and flows via the Reynolds stress in order to understand the L-H transition.

The analysis then proceeded to evaluate the energy exchange dynamics across the L-H transition. More specifically, we investigated the exchange dynamics on NSTX discharges and results can be summarized into three points.

- The relative GPI fluctuation decreased rapidly and consistently across the L-H transition, as shown in figs. 1(a) & 2(a), which is consistent with many previous experimental results at the L-H transition. However, there were no consistent changes *preceding* the L-H transition in the relative fluctuation level, the average poloidal or radial correlation lengths, the average poloidal or radial velocities, or the average poloidal flow shear, as shown in figs. 2(b) & (c), 4, and figs 6(b), 7(b), & 8(b). This absence of a precursor or “trigger” signal preceding the transition is also a relatively common result, but is shown here for NSTX in a clear way over a large database. Finally, these turbulence quantities do change from before to after the transition, as would be expected from the well-known edge profile changes, but this does not help to identify the L-H transition mechanism.
- We then proceeded to the examination of energy transfer via the Reynolds stress and production term. This analysis was performed using a newly implemented velocimetry approach (ODP) to obtain the radial and poloidal velocities with better temporal and spatial resolution than TDE. We use three approaches to examine the transfer dynamics.
 - **We computed the production term in a region corresponding to the H-mode pedestal (1 cm inside the separatrix). We systematically inferred a negative production term, which suggests an energy transfer from mean flows to turbulence. The inferred sign is inconsistent with fluctuation level drops across the L-H transition and with the predator-prey model.**
 - **This discrepancy, along with the significant uncertainties inherent to the velocity analysis, motivated theoretical work [11]. The key aspect of this model is to include the parallel electron dynamics and the thermal free energy, consistent with the original predator-prey model, Ref. [5]. The key result is that in order for Reynolds work to suppress the turbulence, it must deplete the total turbulent free energy, including the thermal free-energy term.** For this to occur, the increase in kinetic energy in the mean flow over the L-H transition must be comparable to the pre-transition thermal free energy. However, this ratio was found to be of order 10^{-2} , even at its maximum (3.5 cm inside the LCFS). **Although there are significant simplifications in the theoretical model, they are very unlikely to cause inaccuracy by two orders of magnitude, suggesting that direct turbulence depletion by the Reynolds work may not be large enough to explain the L-H transition on NSTX, contrary to the predator-prey model.**
 - Finally, we examine the absolute value of the production term to assess its contribution to

330 the duration of the L-H transition and found that given our inferred absolute value of the 330
331 production term, the L-H transition duration should be about 18 ms, which is far too long 331
332 compared **to the experimentally estimated duration of around 100 μ s**. Alternatively, 332
333 we computed the ratio of the Reynolds work to the change of thermal free energy, **which was** 333
334 found to be much less than 1. **Despite uncertainty due to velocimetry and theoretical** 334
335 **modeling, the very large discrepancy suggests that the production term cannot** 335
336 **cause the change in thermal free energy on NSTX, as would be required for** 336
337 **turbulence depletion.** 337

- 338 • Nonnegligible contribution to the poloidal flows by the Reynolds stress, however, is plausible given 338
339 the comparable magnitude of the measured mean poloidal flows with the estimated Reynolds-stress- 339
340 driven flows. 340

341 In summary, this analysis suggests that turbulence depletion by Reynolds work is probably not the 341
342 mechanism of the L-H transition in NSTX, but no alternative mechanism was found from either the 342
343 experimental data or from the new model. However, there are still significant uncertainties in the analysis 343
344 and interpretation of the 2-D velocity fields derived from the GPI data, especially during the H-mode 344
345 phase, which can be reduced with additional measurements and quantitative comparisons with turbulence 345
346 simulations. 346

347 This work is supported by U.S. Dept. of Energy contract DE-AC02-09CH11466. 347

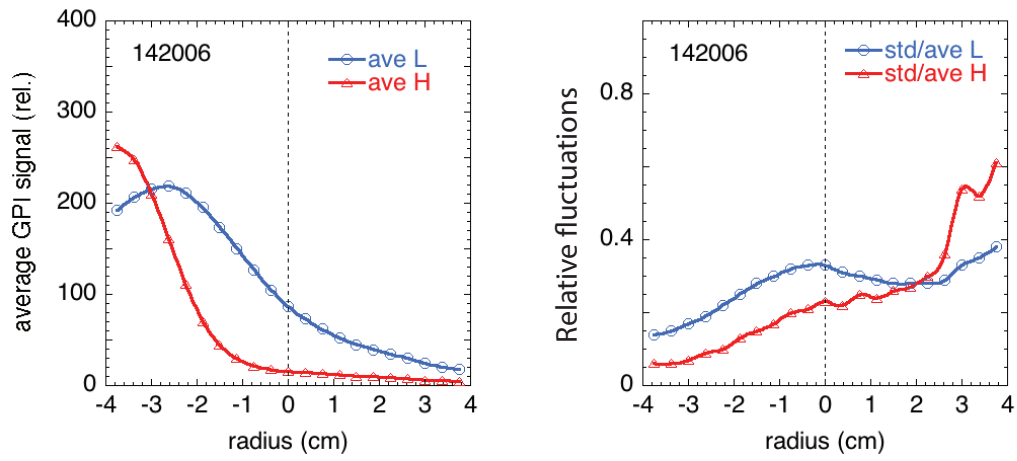


FIG. 1: (Color online). Radial profiles of the GPI signal (left panel) and its relative fluctuation level (right panel), averaged over the L and H-mode periods for the RF discharge 142006. The radial profiles change in response to rapid electron density and temperature changes at the transition. The relative fluctuation level decreases by about a factor-of-two inside and near the separatrix. The dashed line represents the separatrix.

TABLE I: DATABASE OF L-H TRANSITION DISCHARGES. THE COLOR CODE INDICATE THE DIFFERENT HEATING SCHEMES DURING THE L-H TRANSITION.

Shot	L-H time [ms]	Btor [kG]	Plasma current [kA]	NBI Power [MW]	RF Power [MW]	Heating Schemes
138113	254.9	4.4	910	1.4	-	NBI
138114	252.5	4.4	910	1.4	-	NBI
138115	243.0	4.4	910	0	-	NBI
138116	251.6	4.4	910	0	-	NBI
138117	245.8	4.4	910	0	-	NBI
138118	249.5	4.4	910	0	-	NBI
138119	268.4	4.4	910	1.2	-	NBI
139955	364.3	4.4	900	1.0	-	NBI
142229	401.8	4.4	800	1.0	-	NBI
141745	227.7	3.6	800	-	-	Ohmic
141746	244.9	3.6	800	-	-	Ohmic
141747	226.5	3.6	800	-	-	Ohmic
141751	235.0	3.6	800	-	-	Ohmic
141919	231.1	4.4	910	-	0.64	RF
141920	241.5	4.4	910	-	0.60	RF
141922	237.5	4.4	910	-	0.73	RF
142006	223.0	4.4	910	-	0.5	RF

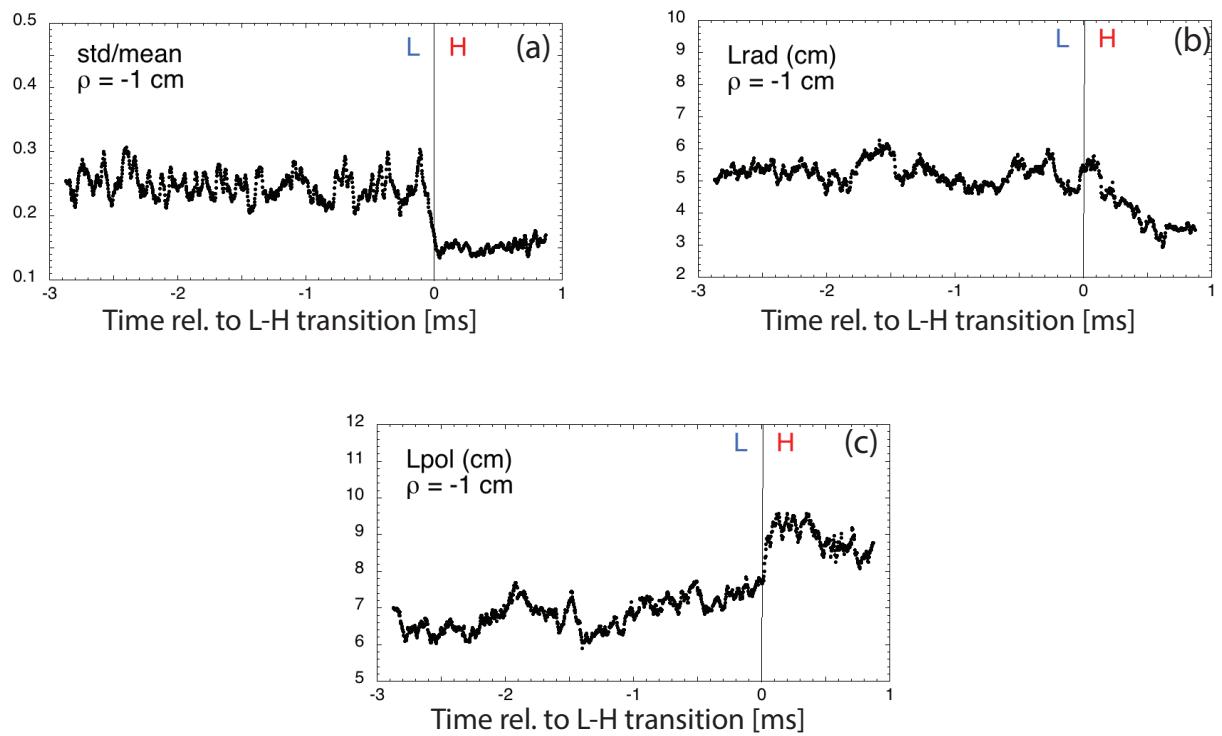


FIG. 2: (Color online). (a) **Relative fluctuation levels for multiple discharges across the L-H transition: the averaged relative fluctuation levels show for all discharges a reduction in fluctuation level across the L-H transition.** (b) **The average radial correlation length decreases after the H-mode transition, and (c) the average poloidal correlation length increases after the transition, averaged over all the discharges at 1 cm inside the separatrix. There are no significant changes in these correlation lengths before the transition.**

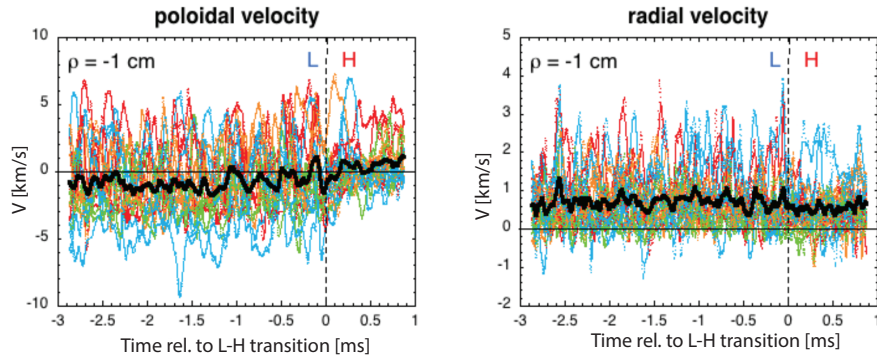


FIG. 3: (Color online) Time dependence of the poloidal and radial velocities for all 17 shots in the database (colored lines), and their averages (black lines), all evaluated at 1 cm inside the separatrix. These velocities are calculated from time-delayed cross-correlation functions averaged over $30 \mu\text{s}$ and 22 cm in the poloidal direction. There is no significant change in the shot-averaged velocities during the 3 ms preceding the L-H transition, but there are slight changes from before to after the transition.

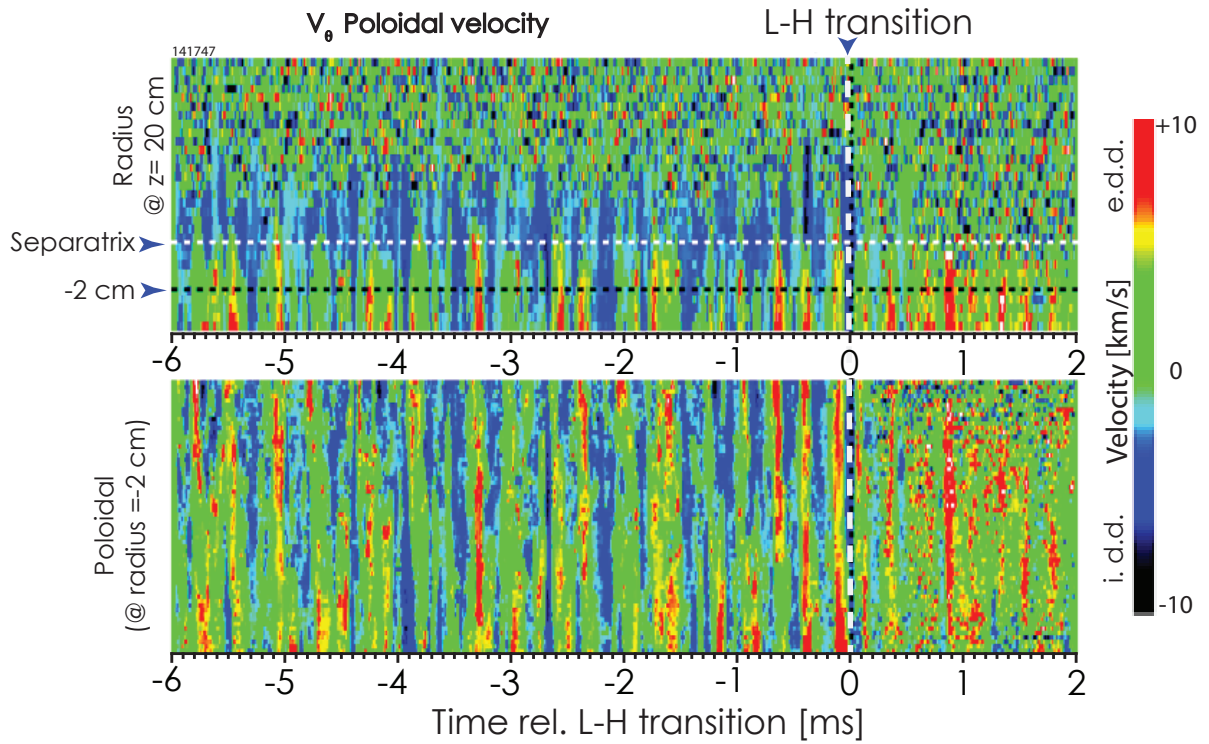


FIG. 4: (Color online) Calculated radial and poloidal profiles of the poloidal velocity vs. time for one shot (141747) based on time-delayed cross-correlation analysis. The magnitude of the poloidal velocity is shown by the color bar at the upper right. There is a poloidal flow oscillation in the radial region near and inside the separatrix (top panel), which often extends 22 cm across the poloidal range of the GPI view (bottom panel), over a time period at least 6 ms before the transition. The radial profile is evaluated near the vertical center of the GPI view, and the poloidal profile is evaluated at 2 cm inside the separatrix for this case.

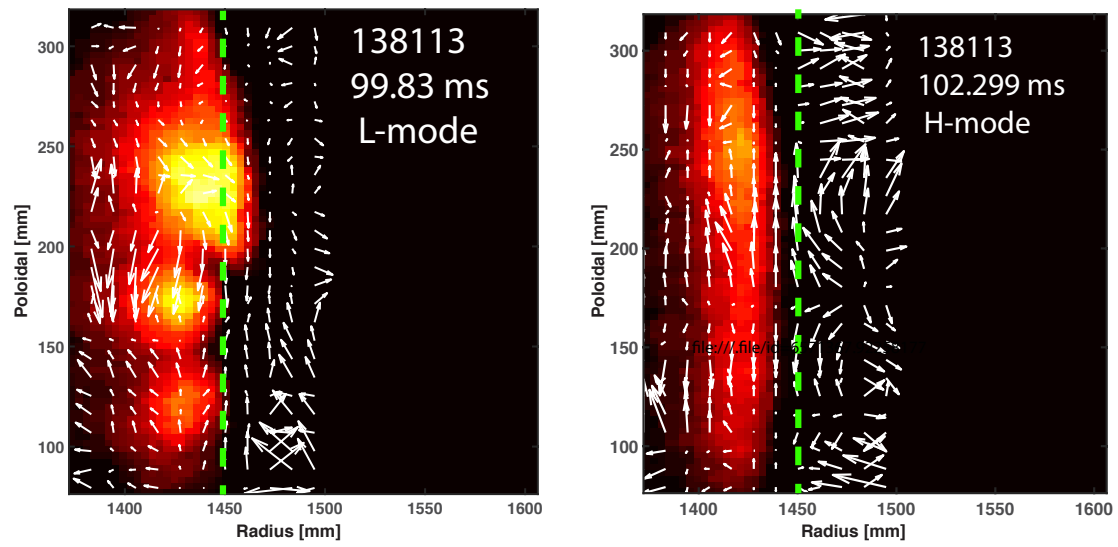


FIG. 5: (Color online). Examples of the GPI intensities images where the arrows represent the velocity vectors. The vertical green dotted line indicates the separatrix location (with ± 1 cm uncertainty).

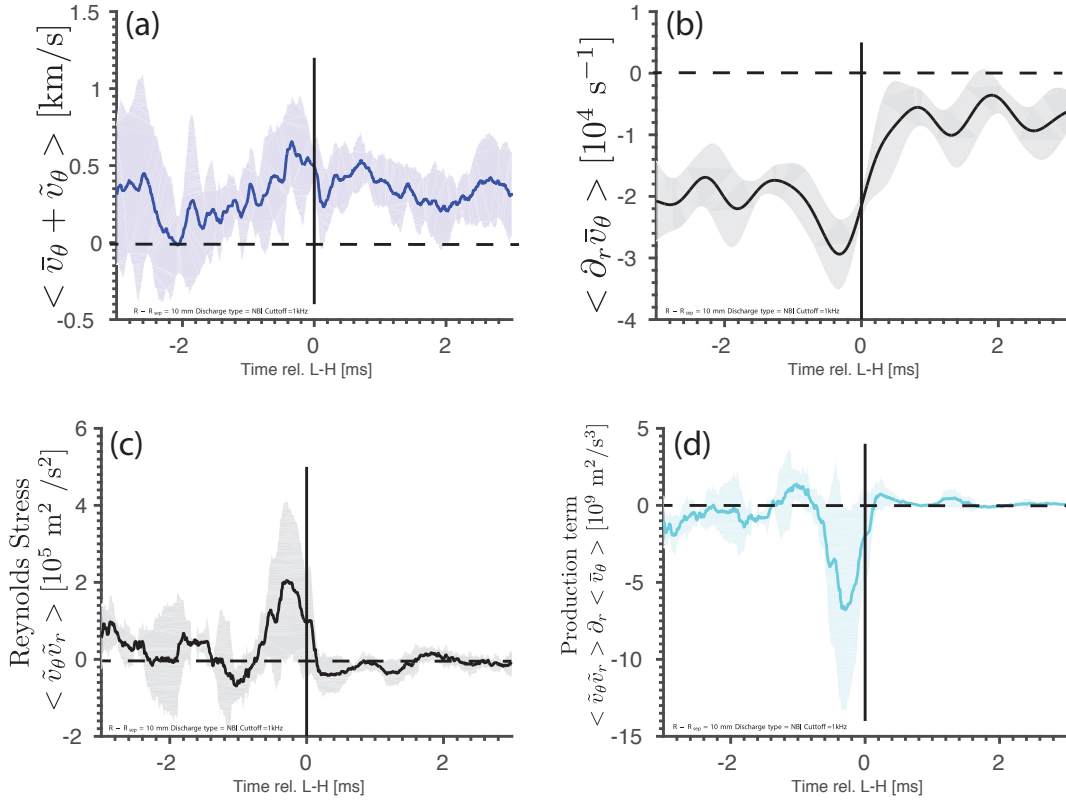


FIG. 6: (Color online). NBI case: flows and derived quantities across the L-H transition at 1cm inside the separatrix. (a) Poloidal flow velocity containing both mean and fluctuating component $\langle \bar{v}_\theta + \tilde{v}_\theta \rangle$. (b) The shear in the mean poloidal flow $\langle \bar{v}_\theta \rangle$ appears to increase across the L-H transition. (c) The Reynolds stress $\langle \tilde{v}_\theta \tilde{v}_r \rangle$ peaks prior to the L-H transition. (d) The production term $\langle \tilde{v}_\theta \tilde{v}_r \rangle \partial_r \langle \bar{v}_\theta \rangle$ is negative during the L-H transition. The shaded area represents the standard deviation from all the NBI discharges.

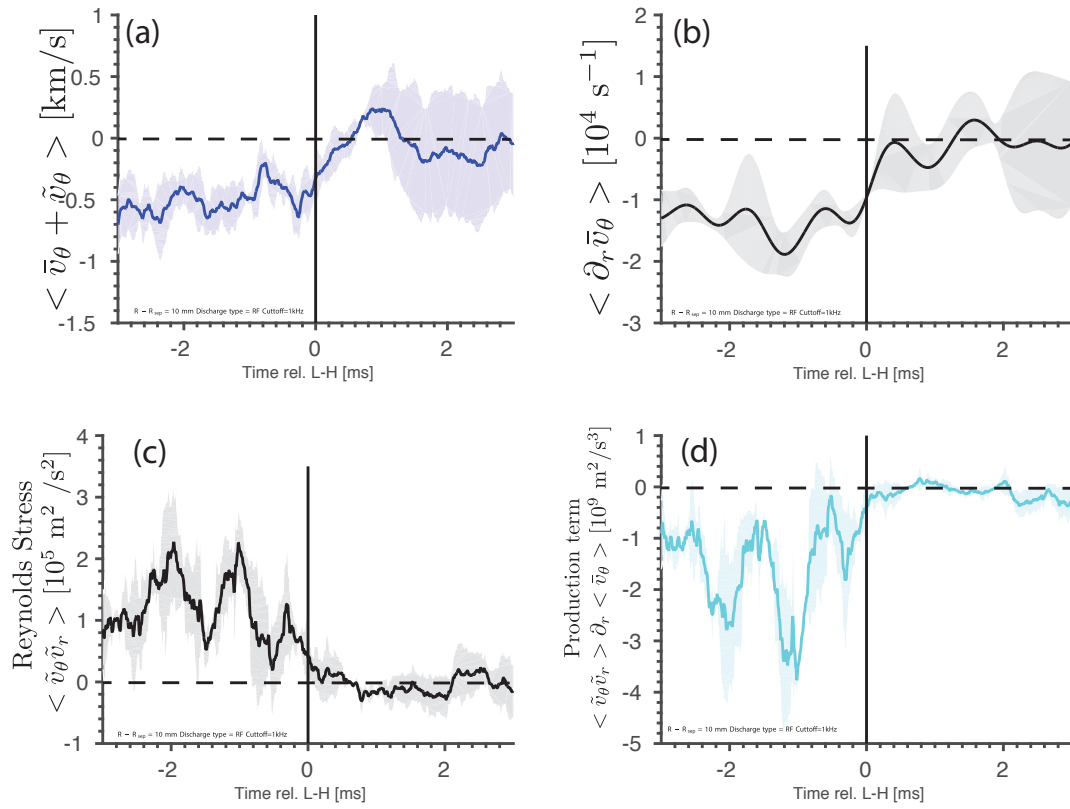


FIG. 7: (Color online). RF case: flows and derived quantities across the L-H transition at 1cm inside the separatrix. See Fig. 6 for captions.

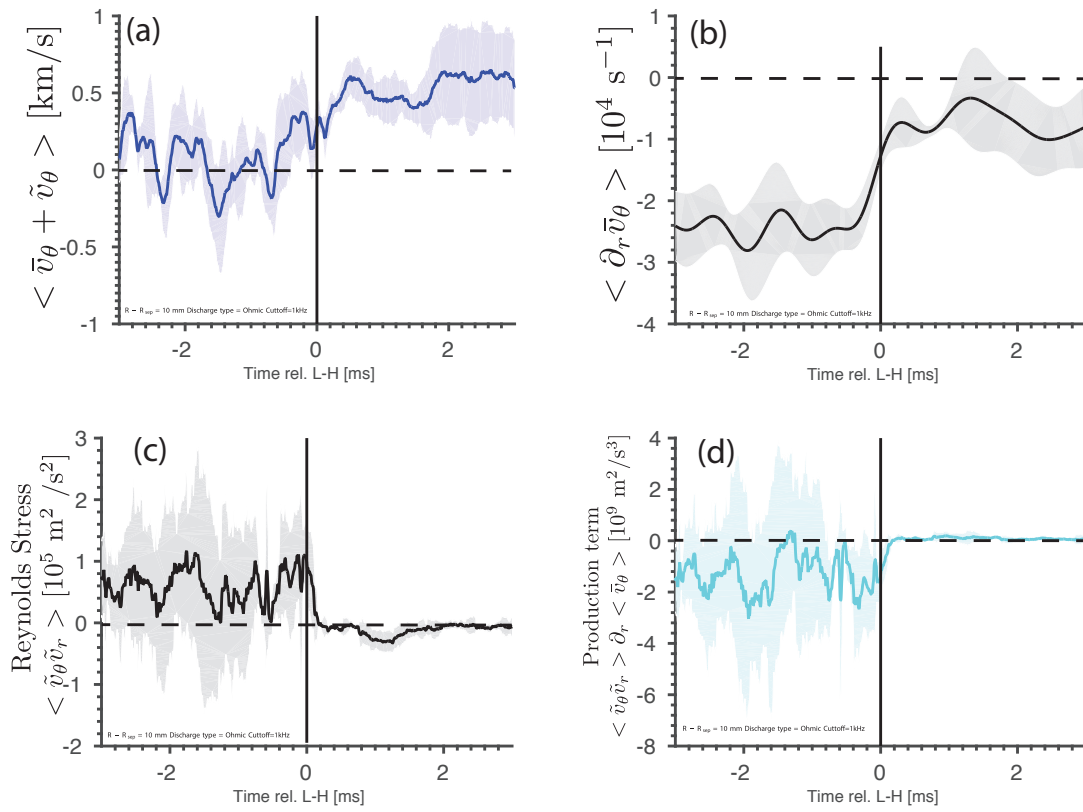


FIG. 8: (Color online). Ohmic case: flows and derived quantities across the L-H transition at 1 cm inside the separatrix. See Fig. 6 for captions.

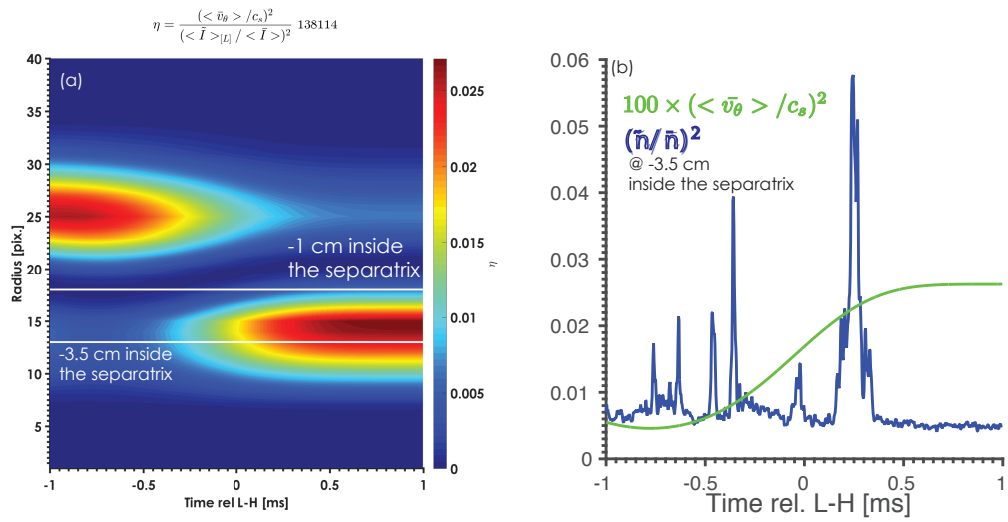


FIG. 9: (Color online). NBI case. Energy ratio of the kinetic energy to the thermal free energy. (a) Radial profile as a function of the time relative to the L-H transition. (b) Time history at 3.5 cm inside the separatrix of the thermal free energy and 100 times the kinetic energy.

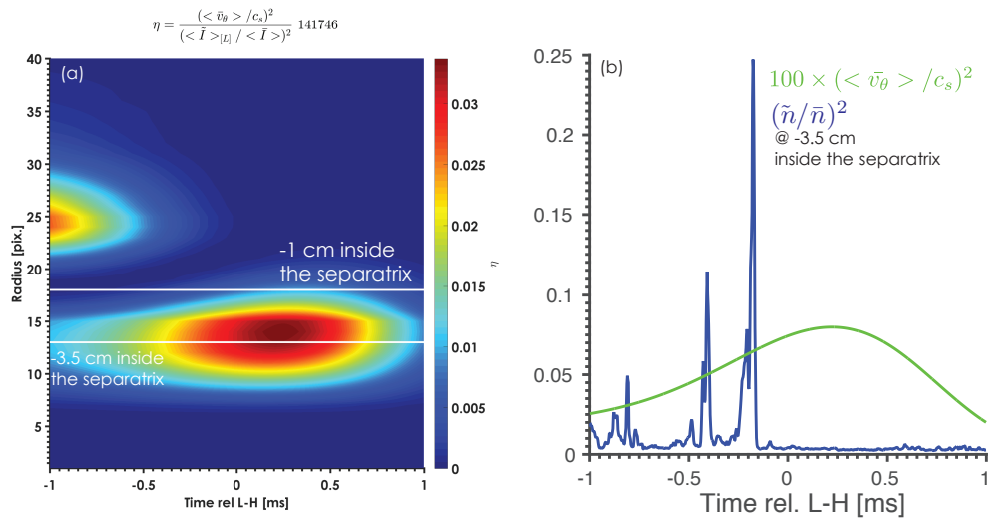


FIG. 10: (Color online). Ohmic case. Energy ratio of the kinetic energy to the free thermal energy. See Fig. 9 captions.

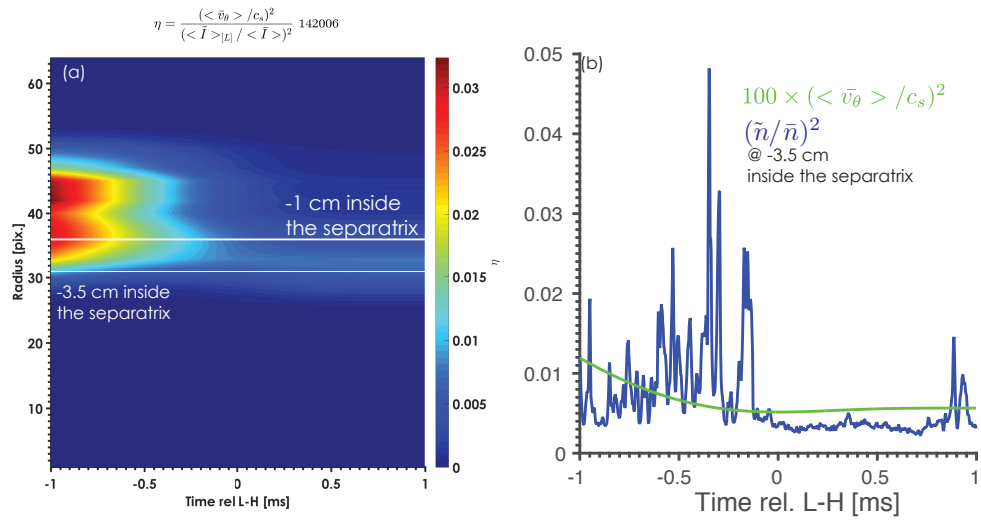


FIG. 11: (Color online). RF case. Energy ratio of the kinetic energy to the free thermal energy. See Fig. 9 captions. Here, the peak of the ratio appears to continuously move inward across the L-H transition.

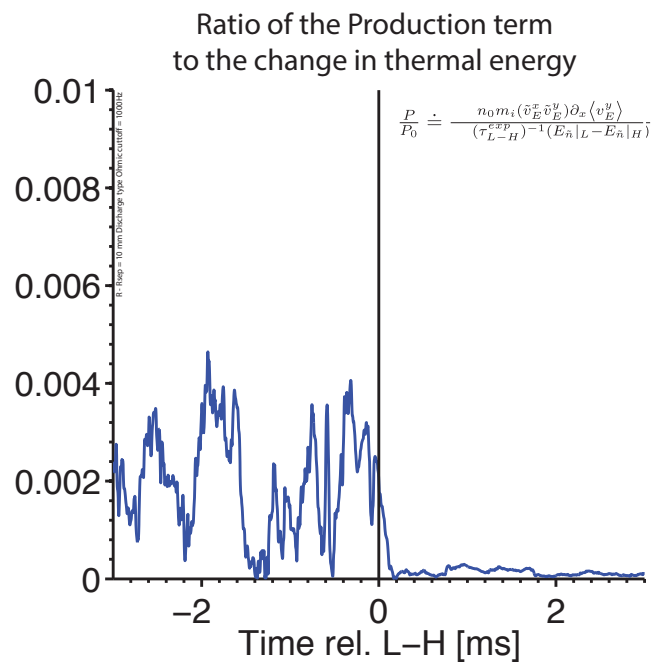


FIG. 12: (Color online). Ohmic case. Ratio of the Reynolds work to the change (in L & H modes) in thermal free energy (see text for discussion.)

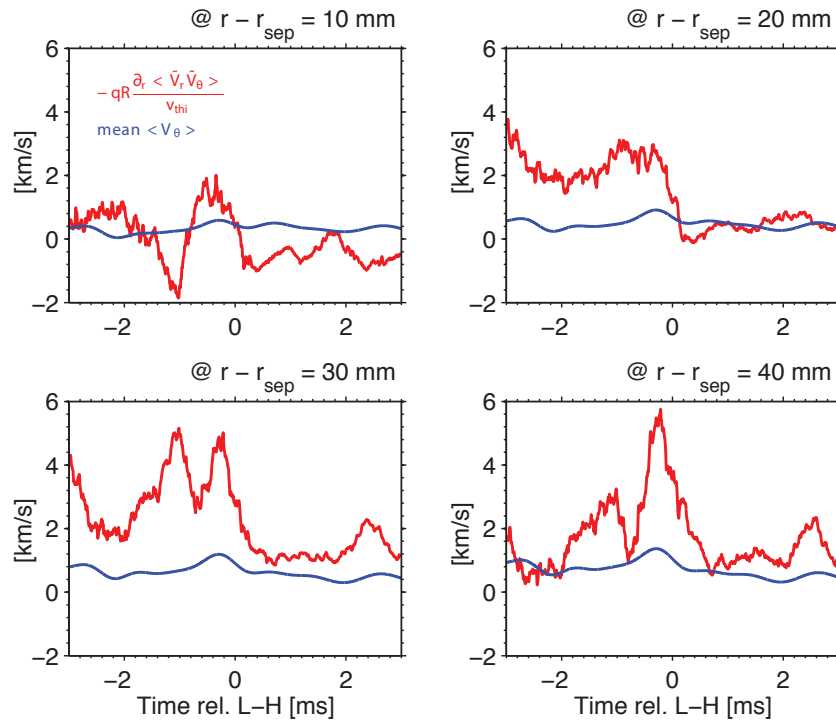


FIG. 13: (Color online). NBI case: the comparison at various radii between the measured mean flow to the estimated Reynolds stress driven flow shows order of magnitude agreement (see text for discussion). Since the Reynolds stress estimate is only good to an order of magnitude, the errorbars have not been included because they might only change the results within an order unity.

References

- 348
- [1] WAGNER, F., BECKER, G., BEHRINGER, K., et al., Phys. Rev. Lett. **49** (1982) 1408. 349
- [2] TEAM, A., Nuclear Fusion **29** (1989) 1959. 350
- [3] BURRELL, K. H., Physics of Plasmas (1994-present) **4** (1997) 1499. 351
- [4] BIGLARI, H., DIAMOND, P. H., and TERRY, P. W., Physics of Fluids B: Plasma Physics **2** (1990) 352
1. 353
- [5] DIAMOND, P. H., LIANG, Y.-M., CARRERAS, B. A., and TERRY, P. W., Phys. Rev. Lett. **72** 354
(1994) 2565. 355
- [6] XU, G., WANG, H., XU, M., et al., Nuclear Fusion **54** (2014) 103002. 356

- 357 [7] YAN, Z., MCKEE, G. R., FONCK, R., et al., Phys. Rev. Lett. **112** (2014) 125002. 357
- 358 [8] CZIEGLER, I., TYNAN, G. R., DIAMOND, P. H., et al., Plasma Physics and Controlled Fusion 358
359 **56** (2014) 075013. 359
- 360 [9] XU, M., TYNAN, G. R., DIAMOND, P. H., et al., Phys. Rev. Lett. **108** (2012) 245001. 360
- 361 [10] SÁNCHEZ, E., HIDALGO, C., GONÇALVES, B., et al., Journal of Nuclear Materials **337–339** 361
362 (2005) 296 , PSI-16. 362
- 363 [11] STOLTZFUS-DUECK, T., Physics of Plasmas **23** (2016) 054505. 363
- 364 [12] SCOTT, B. D., Physics of Plasmas **14** (2007) 102318. 364
- 365 [13] SCOTT, B., Physics of Plasmas **17** (2010) 102306. 365
- 366 [14] NOVAKOVSKII, S. V., LIU, C. S., SAGDEEV, R. Z., and ROSENBLUTH, M. N., Phys. of Plasmas 366
367 **4** (1997) 4272. 367
- 368 [15] SCOTT, B. D., New Journal of Physics **7** (2005) 92. 368
- 369 [16] ZWEBEN, S. J., MAQUEDA, R. J., TERRY, J. L., et al., Physics of Plasmas **13** (2006) 056114. 369
- 370 [17] ZWEBEN, S., DAVIS, W., KAYE, S., et al., Nuclear Fusion **55** (2015) 093035. 370
- 371 [18] ZWEBEN, S. J., MAQUEDA, R. J., HAGER, R., et al., Physics of Plasmas **17** (2010) 102502. 371
- 372 [19] SECHREST, Y., MUNSAT, T., D'IPPOLITO, D. A., et al., Physics of Plasmas **18** (2011). 372
- 373 [20] MCKEE, G. R., FONCK, R. J., GUPTA, D. K., et al., Review of Scientific Instruments **77** (2006) 373
374 10F104. 374
- 375 [21] HIRSCH, M., HOLZHAUER, E., BALDZUHN, J., KURZAN, B., and SCOTT, B., Plasma Physics 375
376 and Controlled Fusion **43** (2001) 1641. 376
- 377 [22] MYRA, J., DAVIS, W., D'IPPOLITO, D., et al., Nuclear Fusion **53** (2013) 073013. 377
- 378 [23] SIERCHIO, J. M., CZIEGLER, I., TERRY, J. L., WHITE, A. E., and ZWEBEN, S. J., Review of 378
379 Scientific Instruments **87** (2016). 379
- 380 [24] BANERJEE, S., ZUSHI, H., NISHINO, N., et al., Review of Scientific Instruments **86** (2015) 033505. 380
- 381 [25] DIALLO, A., CANIK, J., GÖERLER, T., et al., Nuclear Fusion **53** (2013) 093026. 381

Princeton Plasma Physics Laboratory Office of Reports and Publications

Managed by
Princeton University

under contract with the
U.S. Department of Energy
(DE-AC02-09CH11466)

P.O. Box 451, Princeton, NJ 08543
Phone: 609-243-2245
Fax: 609-243-2751

E-mail: publications@pppl.gov

Website: <http://www.pppl.gov>